Available online at www.sciencedirect.com
ScienceDirect
Trans. Nonferrous Met. Soc. China 32(2022) 2480−2493
Transactions of Nonferrous Metals Society of China
www.tnmsc.cn

Influence of rotational speed in friction surfacing of nickel-aluminide reinforced aluminum matrix composite on commercially pure aluminum

Mobina YOUSEFI, Hamed JAMSHIDI AVAL

Department of Materials Engineering, Babol Noshirvani University of Technology, Shariati Avenue, Babol 47148-71167, Iran

Received 3 August 2021; accepted 29 December 2021

Abstract: The effect of rotational speed in the friction surfacing of nickel-aluminide reinforced Al−Zn−Mg−Cu alloy matrix composite on commercially pure aluminum was investigated. The nickel-aluminide reinforcement was fabricated by in-situ methods based on adding nickel powders to Al−Zn−Mg−Cu alloy melt during the semi-solid casting process. The findings showed that an increase in the rotational speed from 600 to 1000 r/min raised the coating efficiency from 65% to 76%. Besides, there was no significant difference between coating efficiencies in the coating with and without nickel-aluminide. The outcomes showed that if the coating was applied at a rotational speed of 1000 r/min, a traverse speed of 100 mm/min, and an axial feeding rate of 125 mm/min, the hardness and shear strength of the substrate increased by up to 225% and 195%, respectively. But the wear rate of the substrate dropped by 75%. Although the hardness of the coating containing nickel-aluminide increases by up to 32% compared to the coating without nickel-aluminide, nickel-aluminide does not affect the thermal stability of the coating.
Key words: nickel-aluminide; aluminum matrix composite; friction surfacing; wear resistance

1 Introduction

Surface engineering is defined as design technologies to protect the surface against undesirable phenomena such as corrosion, wear, and oxidation [1,2]. There are various methods for coating aluminum alloys, such as laser and plasma. However, these methods often have limited applications, which are not economically viable. Since the fusion-based methods are dealt with various shortcomings and limitations, researchers have focused on developing solid-state techniques. Indeed, the solid-state methods occur at temperatures below the melting point of the material. Thus, these are not dealt with problems such as solidification cracks and cavities. In this regard, KLOPSTOCK and NEELANDS in 1941 [3] proposed the friction surfacing (FS) technique as a novel solid-state coating method. In this approach, similar and dissimilar metals are coated on themselves through a strong metallurgical bond and a fine-grained microstructure [3,4].

Besides, metal matrix composites (MMCs) have attracted the attention of researchers in various industries such as military, transportation, and aircraft because of their unique properties [5−9]. These composites, like other composites, are composed of two or more components that play a crucial role in determining their properties. Over the years, many researchers have examined the influence of the FS process on coating a metal rod in a metal substrate [10,11]. However, few studies have evaluated the effect of the FS process parameters on creating an MMC coating.

SHARMA et al [12] employed the FS method for coating the reinforced aluminum matrix composite with 5−10 nm graphene particles on the

Corresponding author: Hamed JAMSHIDI AVAL, Tel: +98-11-35501800, Fax: +98-11-35501808, E-mail: h.jamshidi@nit.ac.ir
DOI: 10.1016/S1003-6326(22)65960-0

AA6061 aluminum surface. The authors reported that the friction coefficient of the coating applied by graphene particles decreased up to 26.76% compared to the substrate. Also, REDDY et al [13] fabricated an AA2124 aluminum matrix composite coating reinforced by SiC particles on the A356 aluminum alloy surface. This procedure has been performed to improve corrosion and wear resistance. In this case, the evidence showed a uniform distribution of SiC particles on the coating under pressure and severe plastic deformation (SPD). OLIVEIRA et al [14] evaluated the friction surfacing of AA6351 aluminum matrix composite (AMC) reinforced with Al_2O_3 particles on AA5052 aluminum alloy substrate. It was observed that after implementing the coating process, the grain size became 48% smaller than the consumable rod. Also, the authors stated that the grains around alumina particles were finer than the other areas. This situation was concerned with acting these particles as nucleation sites and increasing the recrystallization rate.

GANDRA et al [15] investigated the FS of AA6082−SiC composite on AA2024 aluminum alloy substrate. They found that the presence of SiC particles prevented the coating from layering and thus increased its wear resistance. NAKAMA et al [16] utilized the FS method to coat AA6061−Al_2O_3 composite on AA6061 aluminum substrate. It was observed that an increase in rotational speed enhanced the coating efficiency. However, this value decreased by increasing the reinforcement. BARAPOUR et al [17,18] evaluated the effect of adding zinc powder on the properties of AA5083 aluminum coating applied on AA5052 substrate. The authors reported a decrease in the grain size. Also, the results showed that the precipitation hardening mechanism had a significant influence on increasing hardness and improving the mechanical properties of the coating. PIRHYATI and JAMSHIDI AVAL [19−21] coated AA2024 aluminum matrix composite reinforced with silver particles on AA2024 aluminum alloy matrix. It was observed that the hardness and strength of the samples containing silver powder were higher than those of samples without silver. This issue occurred due to the distribution of silver-rich particles and forming intermetallic compounds between silver and aluminum.

According to the scientific resources, inserting the reinforcing particles into the consumable rod through drilling holes within the consumable rod prevents the coating achievement with uniform distribution of reinforcing particles. In this case, the distribution of particles depends on the design of holes. Also, nickel aluminides are the desired choices for the reinforcement particles in fabricating MMCs, due to the properties such as high strength, high corrosion resistance, excellent oxidation resistance at high temperatures, and high elastic modulus [22,23]. In the present study, an AMC rod reinforced with nickel-aluminide was produced by the semi-solid casting method to fabricate a composite coating with uniform distribution of reinforcing particles. Then, the AMC rod was applied to the AA1050 substrate via the FS process. Finally, the rotational speed effect was evaluated on the microstructure, mechanical, and tribological properties of the coating.

2 Experimental

In this study, Al−Zn−Mg−Cu alloy composite reinforced with nickel-aluminide particles was chosen as a consumable rod. Besides, an AA1050 aluminum alloy sheet with a thickness of 4 mm was selected as a substrate. Also, the Al−Zn−Mg−Cu alloy composite rod reinforced with nickel-aluminide particles was produced by a semi-solid casting process developed in Ref. [24]. For this purpose, Al−Zn−Mg−Cu alloy with a chemical composition of 0.03% Si, 0.03% Fe, 1.63% Cu, 6.61% Zn, 3.12% Mg, 0.18% Cr, and Al balance (wt.%) was utilized as a matrix. Also, AA1050 aluminum alloy with a chemical composition of 0.07% Si, 0.28% Fe, 0.05% Cu, 0.01% Mg, 0.02% Mn, and Al balance (wt.%) and the dimensions of 10 cm × 10 cm was used as substrate. In addition, nickel powder with a particle size of <100 μm and a mass fraction of 5% was employed as reinforcement (Fig. 1). In this procedure, the mixture of melt and nickel powder was stirred at a temperature of 630 °C for 10 min. Then, casting was implemented in a cylindrical metal mold with a diameter and length of 3 and 20 cm, respectively. Next, the cast rods were machined to create consumable rods with a diameter and length of 20 and 100 mm, respectively. Afterward, the FS process was performed using a rotational speed of 400−1200 r/min, a traverse speed of 100 mm/min,

and an axial feeding rate of 125 mm/min. Table 1 provides sample labeling according to the process parameters.

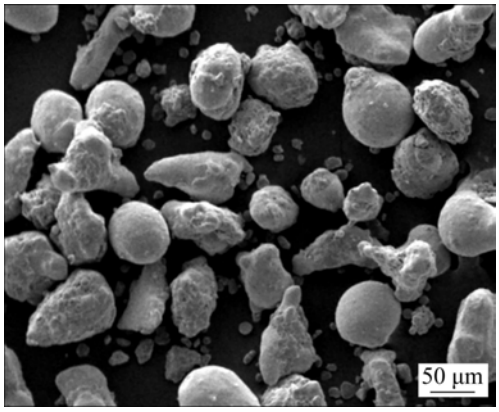

Fig. 1 SEM micrograph of Ni reinforcement used in this study

Table 1 Consumable rod and coated samples labeling

Sample	Rotational speed/ ($r\cdot min^{-1}$)	Traverse speed/ ($mm\cdot min^{-1}$)	Axial feeding rate/ ($mm\cdot min^{-1}$)	Consumable rod
S1	400	100	125	AA7075−5wt.%Ni
S2	600	100	125	AA7075−5wt.%Ni
S3	800	100	125	AA7075−5wt.%Ni
S4	1000	100	125	AA7075−5wt.%Ni
S5	1200	100	125	AA7075−5wt.%Ni
S6	1000	100	125	AA7075
S7	As-cast AA7075−5wt.%Ni consumable rod			
S8	As-cast AA7075 consumable rod			

After implementing the FS process, the coated samples were cut along the perpendicular direction to the coating direction to analyze the coating cross-section (Fig. 2). As shown in Fig. 2, the wear samples were prepared via the coating. The wear properties of the coating were evaluated by the ASTM G99 — 05 standard and applying the pin-on-disk (POD) Tribo-testing machine over a distance of 1000 m. This process was accomplished using AISI 52100 steel counterface disc. Besides, these samples were prepared as a rectangular cube with a square cross-section. Also, these had a diameter of 5 mm in the direction perpendicular to the coating surface.

After grinding and polishing of metallographic samples, the microstructures of the samples were specified using Keller etchant solution with a chemical composition of 95 mL distilled water, 1.5 mL HCl, 1 mL HF, and 2.5 mL HNO_3. Then, this microstructure was examined using an NGF−120A optical microscope and scanning electron microscopy (FEI SEM QUANTA 200). Afterward, the shear punch test (SPT) and micro-hardness test were performed to assess the mechanical properties of the coating. According to the ASTM E92 standard, the hardness of coatings was measured by KOOPA-UV1 universal hardness tester and applying a load of 100 g for 10 s. The distance between indentations was 0.2 mm. The SPT was conducted by a punch speed of 0.001 mm/s based on the method proposed in Ref. [25]. According to Refs. [26−28], the temperature of the $\eta(MgZn_2)$ precipitation was around 200 °C. Therefore, the thermal stability of the coating was evaluated after solid solution treatment at 480 °C. Besides, the artificial aging treatment was performed at 170 °C for different time. Also, the coating hardness was measured to assess the thermal stability.

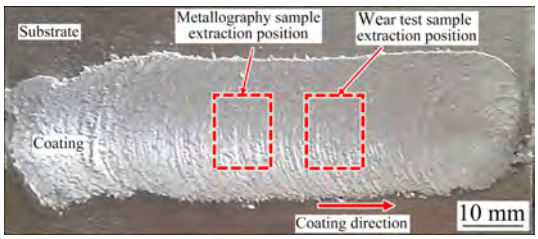

Fig. 2 Microstructural examination, and wear test samples extraction position

3 Results and discussion

3.1 Evaluation of microstructure

Figure 3(a) depicts the effect of rotational speed on the geometric parameters of the coating. As shown in this figure, the rotational speed increment from 1000 to 1200 r/min and its reduction from 600 to 400 r/min did not cause an effective coating on the substrate surface. However, at the rotational speed of 600−1000 r/min, the height and width of the coating decreased by reducing the rotational speed. Also, the rotational speed reduction from 1000 to 600 r/min declined the height and effective width of the coating by 1.17 and 17.81 mm, respectively. The FS process has a

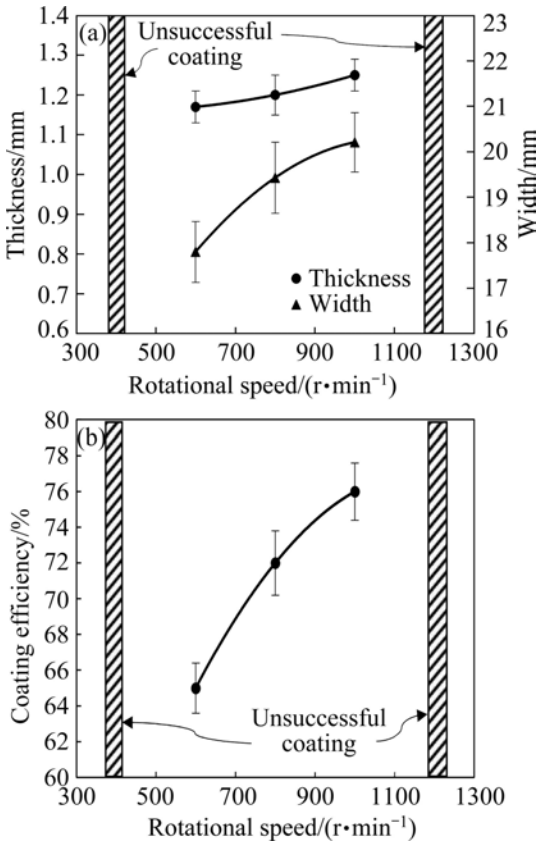

Fig. 3 Effect of consumable rod rotational speed on thickness and width (a) and efficiency (b) of coating at axial feeding rate of 125 mm/min, and traverse speed of 100 mm/min

complex mechanism that can establish the principles of hot working and friction welding [29]. Also, the existing friction between the consumable rod and the substrate generates a viscoplastic zone at the interface of the rod and substrate. Although this zone is in a solid-state, the three-dimensional material flow formed in this zone allows the joint to be made [30]. The sum of the velocity components plays a decisive role in forming the joint at the interface. This issue is due to the rotational speed, traverse speed, and axial feeding rate of the consumable rod. If the rotational speed increases from 600 to 1000 r/min, the heat generated by friction and plastic deformation is enhanced, leading to plastic deformation in more materials. As a result, the volume of deposited materials on the substrate surface increases. A similar result has been reported by other researchers [31−34]. Also, the effect of process parameter has been evaluated on the coating efficiency. In this case, the coating efficiency has been calculated using the equations presented in Ref. [3]. The coating efficiency (η_{coating}) is obtained using Eq. (1):

$$\eta_{\text{coating}} = \frac{W_{\text{a}}}{W_{\text{b}}} \cdot \frac{AV}{\pi r^2 S} \tag{1}$$

where W_{a} and W_{b} are the bonded and maximum coating widths, respectively. Also, A is the area of the coating cross-section (determined by multiplying the width and height of the coating layer), S is the traverse speed, V is the axial feeding rate, and r is the radius of the consumable rod. As shown in Fig. 3(b), an increase in the rotational speed from 600 to 1000 r/min enhanced the coating efficiency from 65% to 76%. Indeed, the coating created by a rotational speed of 1000 r/min, traverse speed of 100 mm/min, and axial feeding rate of 125 mm/min had the highest coating efficiency. Also, the nickel-aluminide-free consumable rod was coated with these parameters, and geometric dimensions of the coating were reported as Sample S5.

The comparison of the coating efficiencies between the two samples of S4 (76%) and S5 (77%) showed no significant difference. In this case, both samples were coated using the same FS parameters. The slight difference between the two samples may be due to the difference between the plastic deformation behaviors of the two consumable rods during the FS process. Since the yield strength of the nickel-aluminide-free consumable rod (104.23 MPa) is less than that of the consumable rod containing nickel-aluminide (121.16 MPa), it is expected that the consumable rod without nickel- aluminide is deformed more than the other one. This situation occurs because of its higher deformation capability during the coating process. Therefore, a coating with greater width and thickness is created, and finally, its coating efficiency becomes higher than the other one.

Figure 4 shows the microstructure of the central zone in various coatings. As shown in this figure, the grain size decreases by increasing rotational speed. Indeed, the average grain size reduces from 4.3 to 2.4 μm by increasing rotational speed from 600 to 1000 r/min. The temperature measurements at the interface between the coating and substrate showed that the rotational speed increment from 600 to 1000 r/min enhanced the temperature from 312 to 351 °C. According to the equations presented in Ref. [35], the rotational

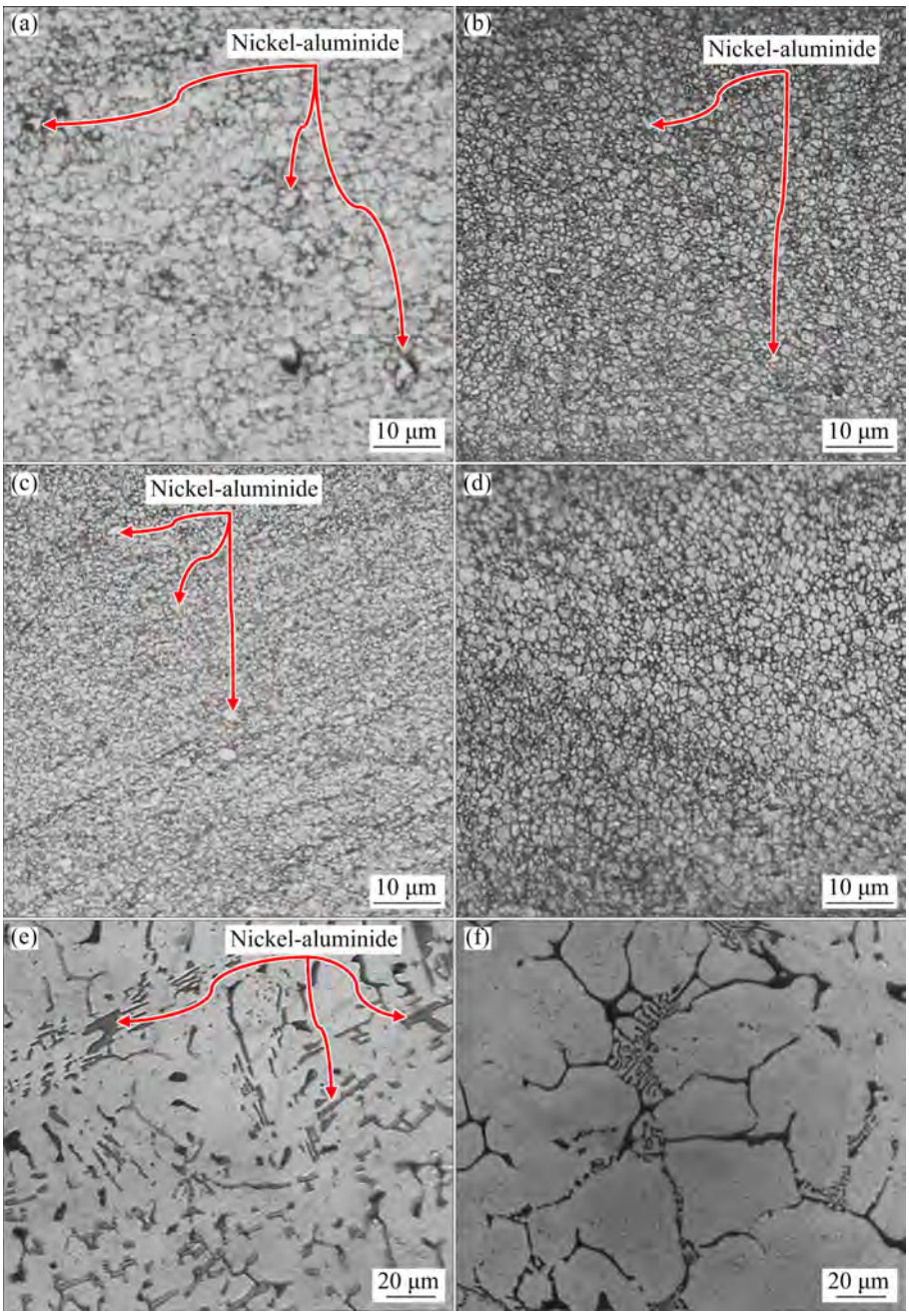

Fig. 4 Microstructures of center zone of coatings: (a) Sample S2; (b) Sample S3; (c) Sample S4; (d) Sample S5; (e) Sample S7; (f) Sample S8

speed increment from 600 to 1000 r/min raised the plastic strain rate from 1213 to 1367 s^{-1}. Overall, the temperature and plastic strain are two crucial factors in the formation of recrystallized microstructure [36,37].

Since the temperature and the plastic strain have an inverse impact on the recrystallized grain size, an increase in the plastic strain and temperature demonstrated that the plastic strain is the predominant factor in decreasing the grain size. Also, a comparison between the microstructures of the two coatings in Samples S4 and S5 has been made. The outcomes showed that the grain size increased from 2.4 to 3.6 μm in the absence of nickel-aluminide particles with the same FS process parameters. Due to severe plastic deformation during the FS process, the reinforcing particles are broken into particles with a size less than 5 μm. Therefore, it is expected that mechanisms such as PSN are activated and create a finer grain size in the coating containing reinforcing particles. In addition, the temperature was measured at the interface

between the coating and substrate in Samples S4 and S5. The outcomes indicated the temperatures of 351 and 362 °C in the samples of S4 and S5, respectively. A decrease in the temperature during the coating process and some mechanisms such as PSN can increase the number of coating grains. Also, these procedures reduce the grain size of the coating.

This study investigated the changes in the morphology, the type of precipitates, and the second-phase particles in different coatings. Figure 5 displays the SEM images for the central zone in the coatings and consumable rods. According to the EDS analysis represented in Fig. 6 and Table 2, the precipitates and particles are Al_2CuMg, Fe-rich particles, nickel-aluminide, and $MgZn_2$. As shown in Fig. 5, the microstructures of the consumable rods and coatings were compared. It was observed that although the morphology and size of the particles and precipitates changed during the FS process, the nature of these particles and precipitates remained constant. Also, Fig. 7 exhibits the average aspect ratios of particles (nickel-aluminide and Fe-rich) in the samples of S2, S3, S4, S5, S7, and S8. These ratios were (0.68, 0.70), (0.70, 0.71), (0.73, 0.75), (Not available, 0.85), (2.40, 1.82), and (Not Available, 1.79) in the samples of S2, S3, S4, S5, S7, and S8, respectively. The SEM

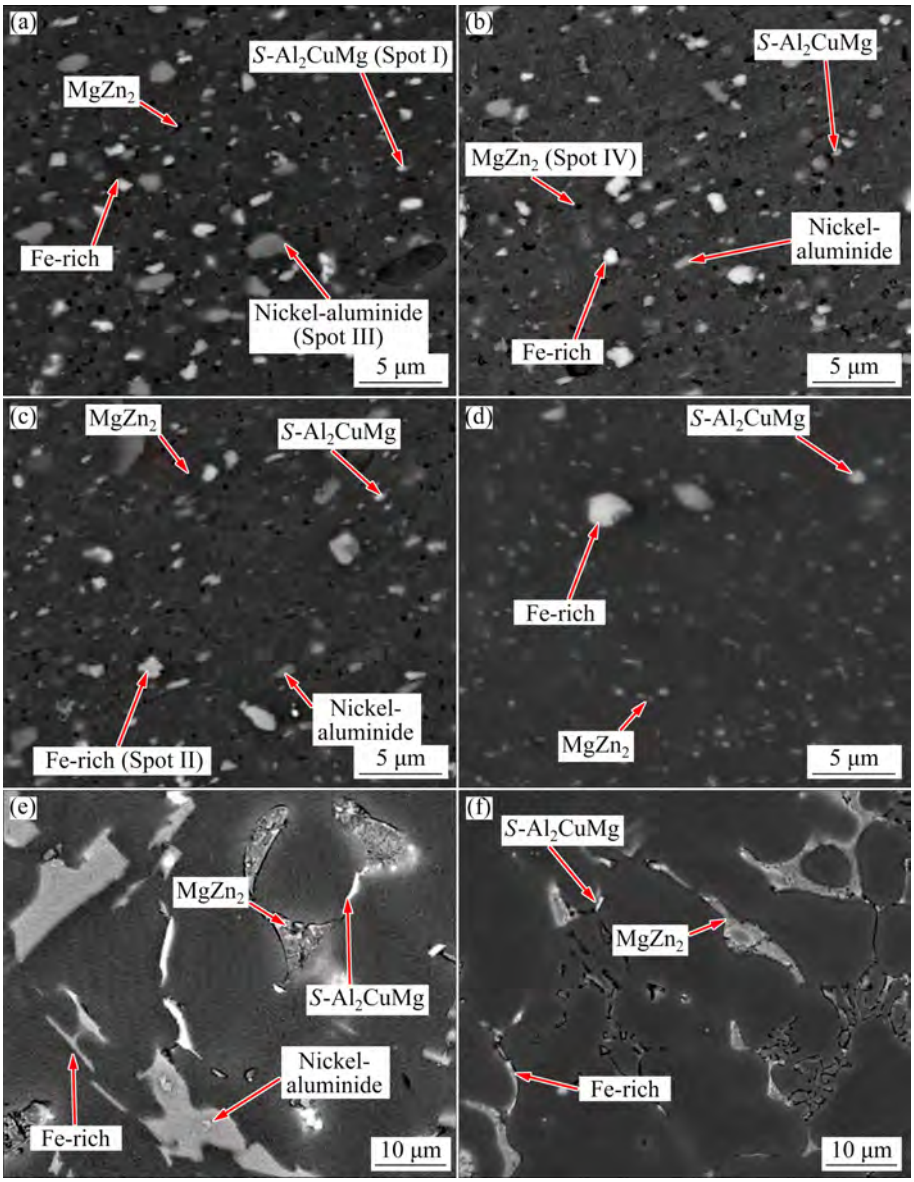

Fig. 5 SEM images of precipitates and second-phase particles at center of coatings: (a) Sample S2; (b) Sample S3; (c) Sample S4; (d) Sample S5; (e) Consumable rod with reinforcement (Sample S7); (f) Consumable rod without reinforcement (Sample S8)

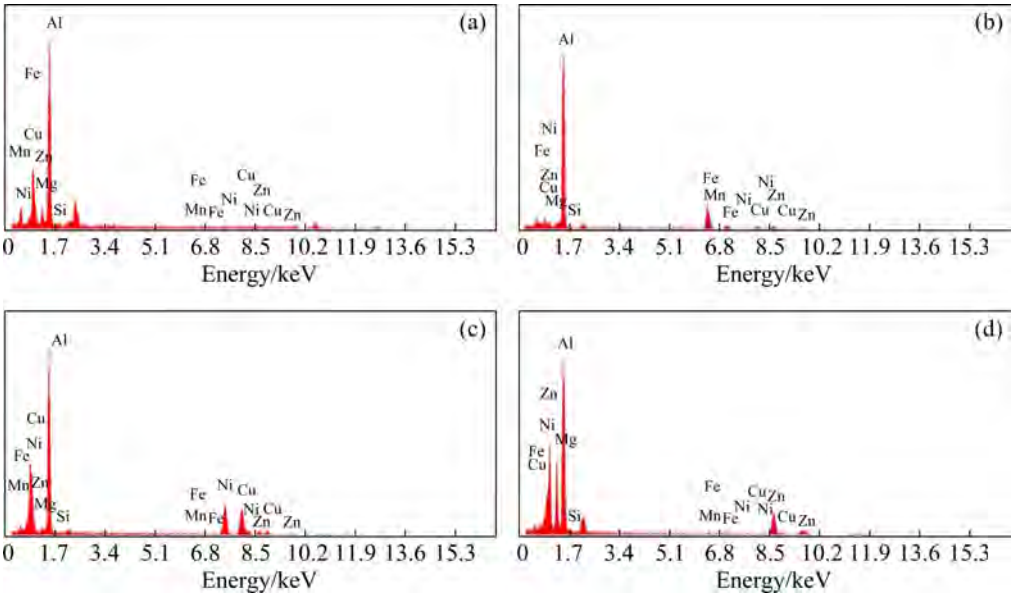

Fig. 6 EDS spectra of Al_2CuMg (Spot I) (a), Fe-rich particle (Spot II) (b), nickel-aluminide (Spot III) (c), and $MgZn_2$ (Spot IV) (d)

Table 2 EDS analysis result of Al_2CuMg (Spot I), Fe-rich particle (Spot II), nickel-aluminide (Spot III), and $MgZn_2$ (Spot IV) (at.%)

Element	Spot I	Spot II	Spot III	Spot IV
Fe	0.44	13.76	0.09	0.21
Mg	10.91	3.14	0.46	14.32
Cu	11.45	1.35	18.07	0.86
Ni	−	−	19.32	0.32
Si	0.51	1.02	0.21	0.78
Mn	0.23	0.31	0.07	0.03
Zn	−	1.93	0.1	28.64
Al	76.46	78.49	61.68	54.84

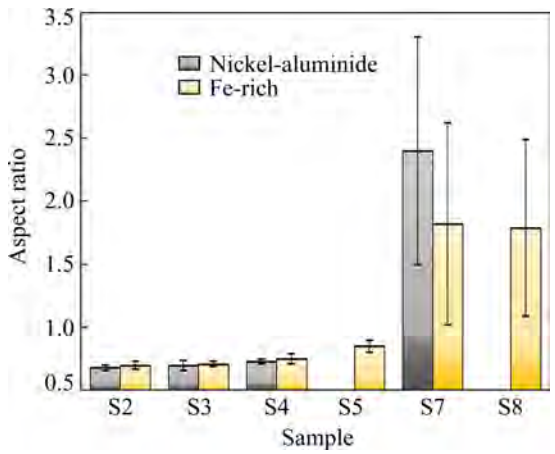

Fig. 7 Aspect ratio of nickel-aluminide and Fe-rich particles in microstructure of consumable rod and coating

images demonstrated that a decrease in the rotational speed from 1000 to 600 r/min increased the sizes of particles and precipitates. In other words, an increase in the rotational speed generates a higher plastic strain rate [33,34,38,39] and enhances the possibility of breaking particles. Since more heat is generated by increasing the rotational speed, the possibility of precipitate dissolution and re-precipitation increases during the FS and cooling processes. Besides, lower temperatures during the process at a rotational speed of 600 r/min prevent the dissolution of precipitates and re-precipitation. In these conditions, the precipitates only grow up.

Figure 8 illustrates the average hardness of coatings, substrates, and consumable rods. The rotational speed reduction from 1000 to 600 r/min due to the increase in the grain size, $\eta(MgZn_2)$ precipitates, and nickel-aluminide (shown in Figs. 4 and 5) decreased the hardness of the coating from (151.2±3.5) to (138.1±2.9) $HV_{0.1}$. In this case, the shear strength of the coating decreased from (289.4±3.8) to (265.3±2.4) MPa. Besides, the samples of S4 and S5 were compared. It was observed that the presence of nickel-aluminide increased the hardness of the coating by up to 32%. Different mechanisms can affect changes in the coating hardness. Since Al−Zn−Cu−Mg alloy is an age-hardenable alloy, precipitation hardening is recognized as one of the effective mechanisms in

changing the strength and hardness. The micro-structural studies revealed that the rotational speed increment due to the smaller precipitates enhanced the strength and hardness.

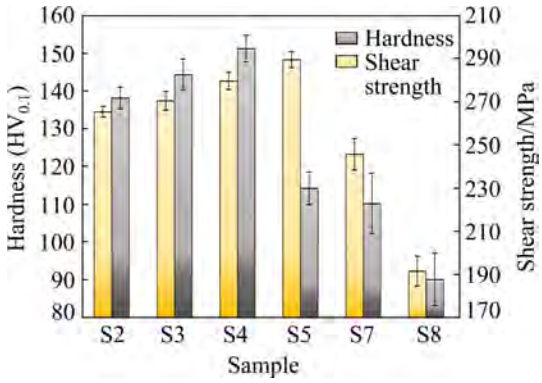

Fig. 8 Variation of average hardness and shear strength of coated samples and consumable rods

The presence of nickel-aluminide particles is another factor that can act as a serious barrier against the movement of dislocations and increase the strength and hardness. With the formation of intermetallic compounds, a difference in the elastic modulus among the constituent phases can be accompanied by other strengthening mechanisms. The dislocation energy can be expressed as a function of the shear modulus of the lattice where it exists [40,41]. As dislocations transfer to a neighboring phase with different shear modulus, the dislocation energy changes. This situation eventually increases the material strength. In other words, strengthening by grain boundaries is another strengthening factor affecting the coating. Indeed, a decrease in the grain size causes the enhancement of the coating hardness. Also, the hardness of the coatings containing and without nickel-aluminide has been compared. In this case, the analysis procedure has been accomplished by computing the simultaneous effect of three factors (i.e., strengthening by precipitates, modulus strengthening, and strengthening by grain boundary) on the hardness and strength of the coatings. The results showed that the coating containing nickel-aluminide had a hardness and strength higher than the coating without nickel-aluminide.

According to Refs. [42−44], the presence of nickel-aluminide compounds can improve the thermal stability of the aluminum alloy matrix. This improvement is due to the high thermal stability of the nickel-aluminides. In this regard, the hardness changes were evaluated based on aging time in the samples of S4 and S5. This procedure has been performed to assess the thermal stability of the coating by implementing long-term heat treatment at 170 °C. Figure 9 depicts the hardness measurements at specific time. As shown in this figure, the hardness increases by enhancing the aging time, and after 2 h, the hardness decreases due to the over-aging phenomenon. Also, it is observed that the nickel-aluminide compounds have a negligible effect on the thermal stability of the coating.

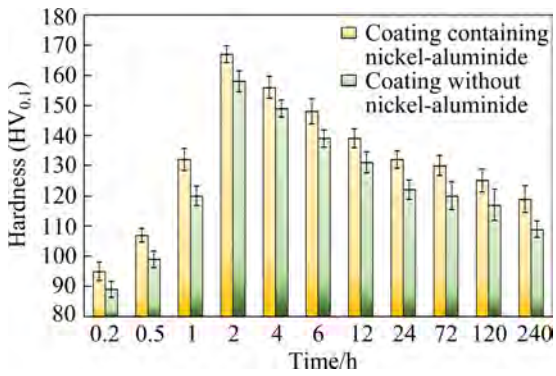

Fig. 9 Variation of hardness of coated samples containing and without nickel-aluminide versus aging time at 170 °C (Both samples coated with rotational speed of 1000 r/min, traverse speed of 100 mm/min, and axial feeding rate of 125 mm/min)

Indeed, the principal factor of strengthening in 7000 series aluminum alloys is $MgZn_2$ precipitates. Therefore, the nickel-aluminide compounds have no impact on the constituents of this precipitate, and only the soluble copper absorption in the aluminum matrix reduces the concentration of this element. It is expected that the precipitation process of the alloy will not change. Also, the SEM and XRD results illustrated in Figs. 10 and 11 confirm that no change in $MgZn_2$ precipitates existed within the two samples (i.e., with and without nickel-aluminide) before and after the aging heat treatment. However, the nickel-aluminide compounds caused larger hardness in the samples containing nickel-aluminide. This situation occurred due to the modulus strengthening mechanism.

3.2 Evaluation of tribological properties

Figure 12 indicates the wear rate and friction coefficient in various samples at the wear distance of 1000 m. This figure plots the variation of friction

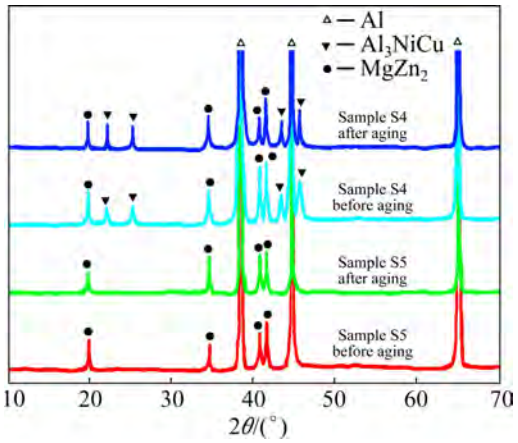

Fig. 10 XRD patterns of Samples S4 and S5 before and after artificial aging for 2 h

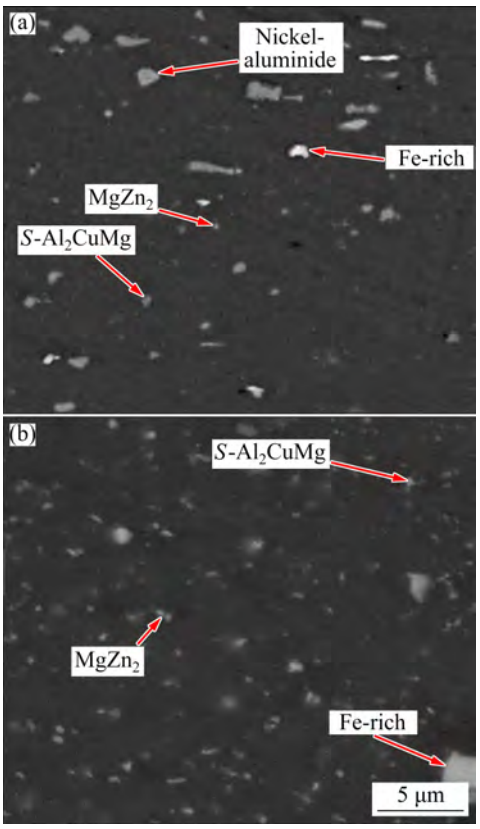

Fig. 11 SEM images of precipitates and second-phase particles of Samples S4 (a) and Sample S5 (b) after artificial aging for 2 h

coefficient against the wear distance. As shown in this figure, the FS process and microstructural modifications reduce the adverse impacts of particles with a large aspect ratio. This procedure improves the wear behavior of the coated samples. Indeed, the microstructure modification reduces the stress concentration created by compounds with a high aspect ratio. Also, the modified compounds

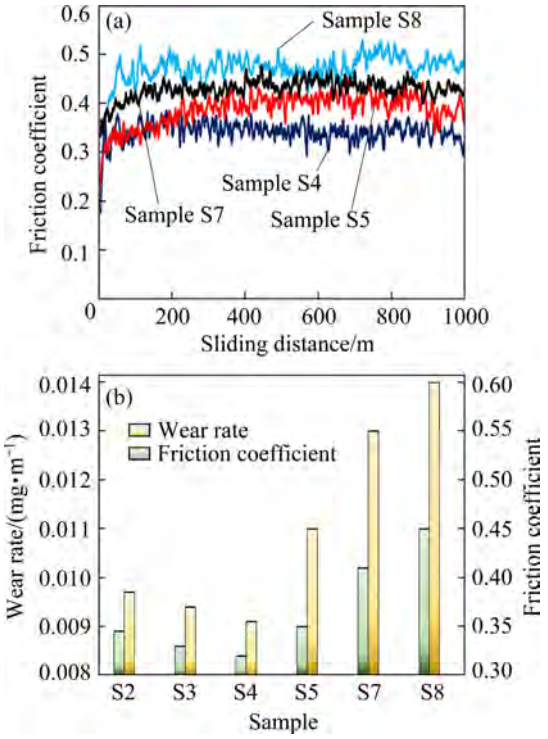

Fig. 12 Variation of friction coefficient versus sliding distance at load of 20 N (a), and wear rate and friction coefficient of different samples (b)

play a strengthening role in this process. Therefore, both approaches increase the strength and wear resistance [45,46]. Overall, the wear rate reduction directly depends on the microstructure, changes in precipitates, and second-phase particles. The rotational speed increment led to the enhancement of the hardness and wear resistance due to the formation of finer precipitates and particles and the smaller grain size in the coating. In this case, the coating without nickel-aluminide (Sample S5) showed a friction coefficient higher than the coatings containing nickel-aluminide.

It is necessary to note that the pin has a greater ability to penetrate conterface in Sample S5. This issue is due to the lack of reinforcing particles. Also, the sides of the pin surface are involved in the conterface, which increases the roughness and friction coefficient. In addition, the friction coefficient curves show that in the initial distances, the coefficient of friction increases due to the small contact surface and oxide layer on the pin surface. Then, the oxide layer is broken, and a complete contact is made between the pin and conterface. In this situation, the friction coefficient decreases and begins fluctuating in a specific range. Since Sample

S4 had a wear resistance higher than other samples, the wear behavior of this sample was investigated under the influence of different applied loads. In this regard, Fig. 13 indicates that the wear resistance decreases by increasing the applied load. This behavior arises from the following reasons. The first reason is concerned with the vertical load.

Indeed, the roughness of the surfaces in contact is plunged into each other and creates a mechanical lock. The second reason is dealt with the formation of the mechanical locks on the surface. In this case, the movement of the surfaces on each other requires the wear of the surface unevenness. Thus, the surfaces are worn. In these conditions, more wear occurs at the surface because of its lower hardness. An increase in the vertical load enhances the entanglement of the surfaces, which are in contact with each other. As a result, the relative movement between the two surfaces causes more surface wear and excessive loss of material.

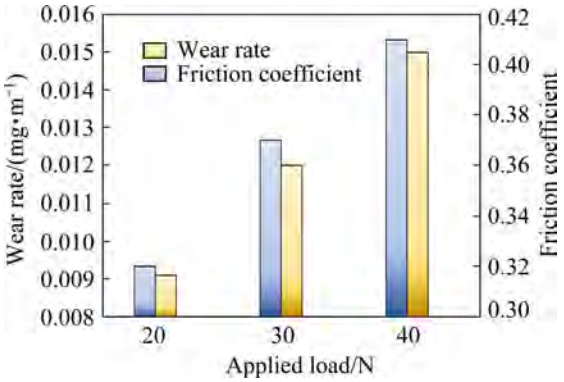

Fig. 13 wear rate and friction coefficient of Sample S4 versus applied load

Figure 14 demonstrates the SEM image of the worn surface in different coatings at an applied load

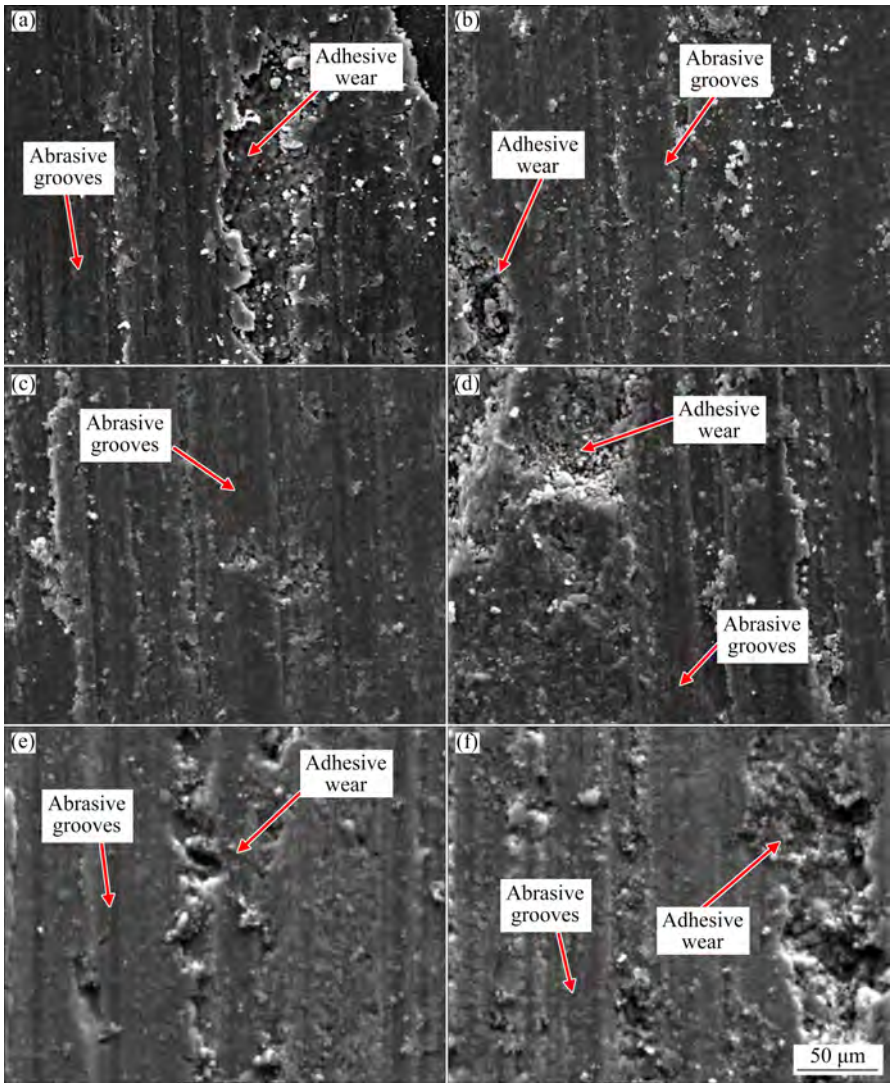

Fig. 14 SEM micrographs of worn surface: (a) Sample S2; (b) Sample S3; (c) Sample S4; (d) Sample S5; (e) Sample S7; (f) Sample S8

of 20 N. The overall features observed on the worn surface exhibit abrasion, adhesion, adhesion joints, and crack formation. Also, the grooves parallel to the slip direction (marked with an arrow) indicate the plowing mode accompanied by fine cuts on the wear surface. In this situation, the wear mechanism is abrasion. In addition, this mechanism is applied in different ways at various time of the wear test. The results showed that there was initially two-body abrasive wear, but the particles were separated from the pin surface and oxidized over time. This process causes three-body abrasive wear. In the three-body abrasive wear, hard particles (i.e., nickel-aluminide reinforcing particles) easily slip or rotate between surfaces, causing abrasion of one or both surfaces. It is concluded that at the load of 20 N, abrasive wear is the predominant mechanism for wear.

Figure 15 exhibits the worn surface of Sample S4 under different loads. In this case, the lamination effects are observed by increasing the applied load. Also, the parallel grooves in the abrasion direction indicate the adhesion mechanism. In addition, the tearing effects on the surface are observed by a further increase of wear load up to 40 N. The dominant mechanism under this load can be attributed to adhesive wear, which causes the plastic deformation on the surface. The plastic deformation

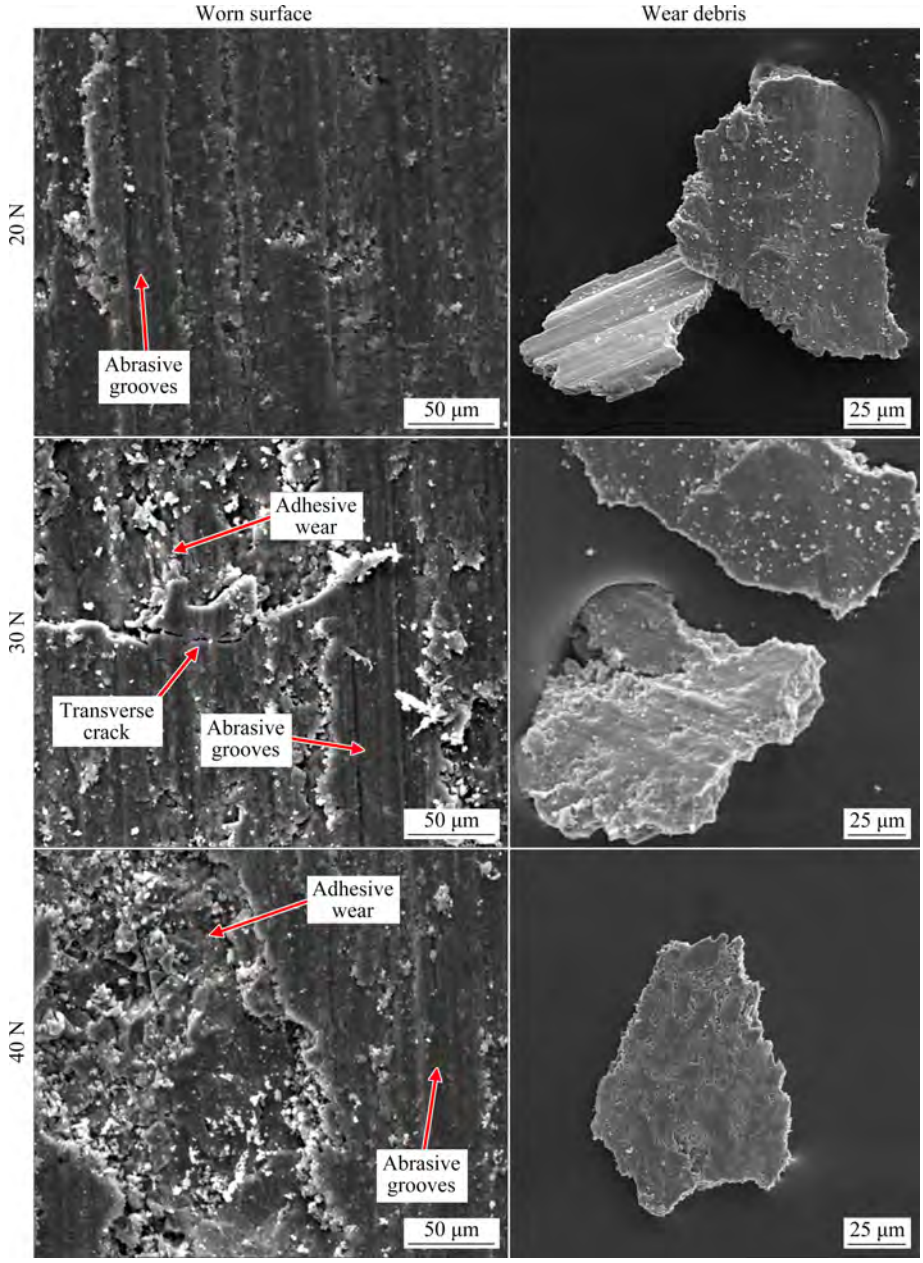

Fig. 15 SEM micrographs of worn surface and wear debris of Sample S4 under different loads

and subsequent crack nucleation/growth in the lower part of the surface create pieces, which can be separated from the surface.

Figure 15 depicts the plate-like debris of the alloy matrix. Microcracks on the surface of debris indicate the resistance reached by the nickel-aluminide. During the rubbing action, some debris gets welded with the conterface disc. If they are detached, the shearing features are shown on the surface. The debris particles probably act as third-body abrasive particles. Also, these are responsible for higher wear rates. In addition, the debris particles trapped among the surfaces cause small plowing on the composite contact surface. The debris contains cracks that occur due to the repeated stress during sliding under load [47,48]. It is necessary to note that the number of these cracks increases by raising the applied load. If the wear load increases, the size of flakes becomes smaller than in other cases. This issue indicates that the matrix becomes softer with a higher load and causes the transition from mild to severe wear. This wear debris represents that the adhesive wear dominates in the sliding direction during wear. Due to the adhesive nature at high load, metal is chipped out in the form of flakes as debris [49].

4 Conclusions

(1) By increasing the rotational speed from 600 to 1000 r/min, the coating efficiency, height, and effective width of the coating increased up to 76%, 1.25 mm, and 20.21 mm, respectively.

(2) By increasing the rotational speed from 600 to 1000 r/min, the average grain size of the coating decreased from (4.3±0.1) to (2.4±0.2) μm. The comparison of the unreinforced and reinforced coatings demonstrated that the nickel-aluminide decreased the average grain size of the coating by 33%.

(3) The microstructure of the consumable rods and coatings revealed that although the morphology and size of the particles and precipitates changed during the FS process, the nature of these particles and precipitates remained constant.

(4) The rotational speed reduction from 1000 to 600 r/min due to the increase in grain size, $\eta(MgZn_2)$ precipitates, and nickel-aluminide decreased the coating hardness from (151.2±3.5) to (138.1±2.9) $HV_{0.1}$. Also, the shear strength of the coating decreased from (279.6±3.8) to (265.3± 2.4) MPa.

(5) The wear rate and friction coefficient in the coating containing nickel-aluminide were 25% and 9% smaller than those of the unreinforced coating.

(6) By increasing the applied load, the adhesive wear was the dominant wear mechanism. Also, the number of cracks on debris increased by raising the applied load. If the wear load increased, the size of flakes became smaller. This situation showed that the matrix became softer with a higher load and caused the transition from mild to severe wear.

References

[1] CHATTOPADHYAY R. Advanced thermally assisted surface engineering processes [M]. Springer Science & Business Media, 2007.

[2] DAVIS J R. Surface engineering for corrosion and wear resistance [M]. ASM International, 2001.

[3] GANDRA J, KROHN H, MIRANDA R M, VILAÇA P, QUINTINO L, DOS SANTOS J F. Friction surfacing — A review [J]. Journal of Materials Processing Technology, 2014, 214(5): 1062−1093.

[4] THOMAS W M, NICHOLAS E D, WATTS E R, STAINES D G. Friction based welding technology for aluminium [J]. Materials Science Forum, 2002, 396−402: 1543−1548.

[5] SHA J J, LÜ Z Z, SHA R Y, ZU Y F, DAI J X, XIAN Y Q, ZHANG W, CUI D, YAN C L. Improved wettability and mechanical properties of metal coated carbon fiber-reinforced aluminum matrix composites by squeeze melt infiltration technique [J]. Transactions of Nonferrous Metals Society of China, 2021, 31(2): 317−330.

[6] NIE Q Q, CHEN G H, WANG B, YANG L, TANG W M. Process optimization, microstructures and mechanical/ thermal properties of Cu/Invar bi-metal matrix composites fabricated by spark plasma sintering [J]. Transactions of Nonferrous Metals Society of China, 2021, 31(10): 3050−3062.

[7] WANG H, ZHANG H M, CUI Z S, CHEN Z, CHEN D. Compressive response and microstructural evolution of in-situ TiB_2 particle-reinforced 7075 aluminum matrix composite [J]. Transactions of Nonferrous Metals Society of China, 2021, 31(5): 1235−1248.

[8] WANG P, ECKERT J, PRASHANTH K G, WU M W, KABAN I, XI L X, SCUDINO S. A review of particulate-reinforced aluminum matrix composites fabricated by selective laser melting [J]. Transactions of Nonferrous Metals Society of China, 2020, 30(8): 2001−2034.

[9] PANDEY N, CHAKRABARTY I, BARKANE K, MEHTA N S, MAJHI M R. Microstructure, mechanical and wear properties of aluminum borate whisker reinforced aluminum matrix composites [J]. Transactions of Nonferrous Metals Society of China, 2020, 30(7): 1731−1742.

[10] ESTHER I, DINAHARAN I, MURUGAN N. Microstructure and wear characterization of AA2124/4wt.%B4C nano-composite coating on Ti−6Al−4V alloy using friction surfacing [J]. Transactions of Nonferrous Metals Society of China, 2019, 29(6): 1263−1274.

[11] SHARMA A, SHARMA V M, PAUL J. A comparative study on microstructural evolution and surface properties of graphene/CNT reinforced Al6061−SiC hybrid surface composite fabricated via friction stir processing [J]. Transactions of Nonferrous Metals Society of China, 2019, 29(10): 2005−2026.

[12] SHARMA A, SAGAR S, MAHTO R P, SAHOO B, PAL S K, PAUL J. Surface modification of Al6061 by graphene impregnation through a powder metallurgy assisted friction surfacing [J]. Surface and Coatings Technology, 2018, 337: 12−23.

[13] REDDY G M, RAO K S, MOHANDAS T. Friction surfacing: Novel technique for metal matrix composite coating on aluminium–silicon alloy [J]. Surface Engineering, 2009, 25(1): 25−30.

[14] OLIVEIRA P H F, GALVIS J C, MARTINS J D P, CARVALHO A L M. Application of friction surfacing to the production of aluminum coatings reinforced with Al_2O_3 particles [J]. Materials Research, 2017, 20: 603−620.

[15] GANDRA J, VIGARINHO P, PEREIRA D, MIRANDA R M, VELHINHO A, VILAÇA P. Wear characterization of functionally graded Al−SiC composite coatings produced by friction surfacing [J]. Materials & Design (1980−2015), 2013, 52: 373−383.

[16] NAKAMA D, KATOH K, TOKISUE H. Fabrication of 6061 aluminum alloy/$A1_2O_3$ particle composites by friction surfacing [J]. Journal of Japan Institute of Light Metals, 2008, 58(7): 299−304.

[17] BARARPOUR S M, JAMSHIDI AVAL H, JAMAATI R. Effects of Zn powder on alloying during friction surfacing of Al−Mg alloy [J]. Journal of Alloys and Compounds, 2020, 818: 152823.

[18] BARARPOUR S M, JAMSHIDI AVAL H, JAMAATI R. Effect of non-isothermal aging on microstructure and mechanical properties of friction surfaced AA5083−15wt.%Zn composites [J]. Surface and Coatings Technology, 2020, 384: 125307.

[19] PIRHAYATI P, JAMSHIDI AVAL H. Effect of silver on non-isothermal aging of friction surfaced AA2024−16wt.%Ag composites [J]. Surface and Coatings Technology, 2019, 379: 125059.

[20] PIRHAYATI P, JAMSHIDI AVAL H. Effect of post-heat treatment on friction surfaced Al−Cu−Mg alloy coating containing Ag [J]. Surface and Coatings Technology, 2020, 397: 125984.

[21] PIRHAYATI P, JAMSHIDI AVAL H. Microstructural characterization and mechanical properties of friction surfaced AA2024−Ag composites [J]. Transactions of Nonferrous Metals Society of China, 2020, 30(7): 1756−1770.

[22] DEEVI S, SIKKA V. Nickel and iron aluminides: an overview on properties, processing, and applications [J]. Intermetallics, 1996, 4(5): 357−375.

[23] LIU F C, ZHU X Z, JI S X. Effects of Ni on the microstructure, hot tear and mechanical properties of Al−Zn−Mg−Cu alloys under as-cast condition [J]. Journal of Alloys and Compounds, 2020, 821: 153458.

[24] KHAKI-DAVOUDI S, NOUROUZI S, JAMSHIDI AVAL H. Microstructure and mechanical properties of AA7075/Al_3Ni composites produced by compocasting [J]. Materials Today Communications, 2021, 28: 102537.

[25] ALIZADEH R, MAHMUDI R. Evaluating high-temperature mechanical behavior of cast Mg−4Zn−*x*Sb magnesium alloys by shear punch testing [J]. Materials Science and Engineering A, 2010, 527(16/17): 3975−3983.

[26] ZHAO Y H, LIU J Z, TOPPING T D, LAVERNIA E J. Precipitation and aging phenomena in an ultrafine grained Al−Zn alloy by severe plastic deformation [J]. Journal of Alloys and Compounds, 2021, 851: 156931.

[27] FOUAD F, NAEEM H T. Investigation on the behavior of the modified AA 7075 alloy using differential scanning calorimetry technique [C]//IOP Conference Series: Materials Science and Engineering. IOP Publishing, 2021.

[28] PIEŁA K, BŁAŻ L, SIERPIŃSKI Z, FORYŚ T. Non-isothermal annealing of AA7075 aluminum alloy−Structural and mechanical effects [J]. Archives of Metallurgy and Materials, 2012, 57(3): 703−709.

[29] SILVÉRIO S, KROHN H, FITSEVA V, de ALCÂNTARA N G, dos SANTOS J F. Deposition of AA5083-H112 over AA2024-T3 by friction surfacing [J]. Soldagem & Inspeção, 2018, 23(2): 225−234.

[30] VILAÇA P, GANDRA J, VIDAL C. Linear friction based processing technologies for aluminum alloys: Surfacing, stir welding and stir channeling [M]//Aluminium Alloys−New Trends in Fabrication and Applications. Tech Rijeka, 2012.

[31] GANDRA J, PEREIRA D, MIRANDA R M, VILAÇA P. Influence of process parameters in the friction surfacing of AA 6082-T6 over AA 2024-T3 [J]. Procedia CIRP, 2013, 7: 341−346.

[32] RAHMATI Z, JAMSHIDI AVAL H, NOUROUZI S, JAMAATI R. Effect of friction surfacing parameters on microstructure and mechanical properties of solid-solutionized AA2024 aluminium alloy cladded on AA1050 [J]. Materials Chemistry and Physics, 2021, 269: 124756.

[33] PIRHAYATI P, JAMSHIDI AVAL H. An investigation on thermo-mechanical and microstructural issues in friction surfacing of Al−Cu aluminum alloys [J]. Materials Research Express, 2019, 6(5): 056550.

[34] BARARPOUR S M, JAMSHIDI AVAL H, JAMAATI R. Modeling and experimental investigation on friction surfacing of aluminum alloys [J]. Journal of Alloys and Compounds, 2019, 805: 57−68.

[35] EHRICH J, ROOS A, KLUSEMANN B, HANKE S. Influence of Mg content in Al alloys on processing characteristics and dynamically recrystallized microstructure of friction surfacing deposits [J]. Materials Science and Engineering A, 2021, 819: 141407.

[36] HUMPHREYS F J, HATHERLY M. Recrystallization and related annealing phenomena [M]. Elsevier, 2012.

[37] ALANEME K K, OKOTETE E A. Recrystallization mechanisms and microstructure development in emerging metallic materials: A review [J]. Journal of Science:

Advanced Materials and Devices, 2019, 4(1): 19−33.
[38] BARARPOUR S M, JAMSHIDI AVAL H, JAMAATI R. An experimental and theoretical investigation of thermo-mechanical issues in friction surfacing of Al−Mg aluminum alloys: Material flow and residual stress [J]. Modelling and Simulation in Materials Science and Engineering, 2020, 28(3): 035003.
[39] RAHMATI Z, JAMSHIDI AVAL H, NOUROUZI S, JAMAATI R. Modeling and experimental study of friction surfacing of AA2024 alloy over AA1050 plates [J]. Materials Research Express, 2019, 6(8): Doi: 10.1088/2053-1591/ab255a.
[40] PANDEY P, MAKINENI S K, GAULT B, CHATTOPADHYAY K. On the origin of a remarkable increase in the strength and stability of an Al rich Al−Ni eutectic alloy by Zr addition [J]. Acta Materialia, 2019, 170: 205−217.
[41] DIXIT M, MISHRA R S, SANKARAN K K. Structure–property correlations in Al 7050 and Al 7055 high-strength aluminum alloys [J]. Materials Science and Engineering A, 2008, 478(1): 163−172.
[42] DEY G K. Physical metallurgy of nickel aluminides [J]. Sadhana, 2003, 28(1): 247−262.
[43] XIANG Z D, ROSE S R, DATTA P K. Long term oxidation resistance and thermal stability of Ni-aluminide/Fe-aluminide duplex diffusion coatings formed on ferritic steels at low temperatures [J]. Intermetallics, 2009, 17(6): 387−393.
[44] JOZWIK P, POLKOWSKI W, BOJAR Z. Applications of Ni_3Al based intermetallic alloys—Current stage and potential perceptivities [J]. Materials, 2015, 8(5): 2537−2568.
[45] DEUIS R L, SUBRAMANIAN C, YELLUP J M. Dry sliding wear of aluminium composites — A review [J]. Composites Science and Technology, 1997, 57(4): 415−435.
[46] DWIVEDI D K. Wear behaviour of cast hypereutectic aluminium silicon alloys [J]. Materials & Design, 2006, 27(7): 610−616.
[47] KUMAR S, PANDEY O P. Role of fine size zircon sand ceramic particle on controlling the cell morphology of aluminum composite foams [J]. Journal of Manufacturing Processes, 2015, 20: 172−180.
[48] TORRANCE A A. The effect of grit size and asperity blunting on abrasive wear [J]. Wear, 2002, 253(7/8): 813−819.
[49] KUMAR S, SHARMA A, ARORA R, PANDEY O P. The microstructure and wear behaviour of garnet particle reinforced Al matrix composites [J]. Journal of Materials Research and Technology, 2019, 8(6): 5443−5455.

转速对商业纯铝基体上摩擦堆焊制备铝化镍增强铝基复合材料涂层的影响

Mobina YOUSEFI, Hamed JAMSHIDI AVAL

Department of Materials Engineering, Babol Noshirvani University of Technology, Shariati Avenue, Babol 47148-71167, Iran

摘　要：研究转速对在商业纯铝机体上用摩擦堆焊制备的铝化镍增强 Al−Zn−Mg−Cu 合金基复合材料涂层性能的影响。通过在半固态铸造过程中，向 Al−Zn−Mg−Cu 合金熔体中加入镍粉，原位制备铝化镍增强相。结果表明，当转速从 600 r/min 增加到 1000 r/min 时，涂覆效率从 65%提高到 76%。此外，铝化镍对涂覆效率无显著影响，当在转速为 1000 r/min、横向移动速度为 100 mm/min、轴向给料速度为 125 mm/min 的条件下制备涂层时，基体的硬度和剪切强度分别提高 225%和 195%，但基体的磨损率下降 75%。与不含铝化镍的涂层相比，含铝化镍涂层的硬度提高 32%，但铝化镍不会影响涂层的热稳定性，。

关键词：铝化镍；铝基复合材料；摩擦堆焊；耐磨性能

(Edited by Bing YANG)